Computers in Biology and Medicine 112 (2019) 103384

Contents lists available at ScienceDirect

Computers in Biology and Medicine

journal homepage: www.elsevier.com/locate/compbiomed

Construction of brain structural connectivity network using a novel integrated algorithm based on ensemble average propagator

Zhanxiong Wu[a], Yun Peng[b], Dong Xu[a], Ming Hong[a], Yingchun Zhang[b,*]

[a] *School of Electronic Information, Hangzhou Dianzi University, Hangzhou, Zhejiang, 310018, China*
[b] *Department of Biomedical Engineering, University of Houston, Houston, TX, USA*

ARTICLE INFO

Keywords:
Ensemble average propagator
High angular resolution diffusion imaging
Diffusion weighted imaging
Structural connectivity
Spherical polar fourier imaging

ABSTRACT

An important task for neuroscience is to accurately construct structural connectivity network of human brain. Tractography constructed based on high angular resolution diffusion imaging (HARDI) provides valuable information of human brain structural connections. Existing algorithms, mainly categorized as deterministic or probabilistic, come with inherent limitations (e.g., fiber direction uncertainty induced by noise, or anatomically unreasonable connections and heavy computational cost). In this study, a novel integrated algorithm was proposed to construct brain structural connectivity network by incorporating the deterministic path planning and probabilistic connection strength estimation, based on ensemble average propagator (EAP). We first estimated EAPs from multi-shell samples using the spherical polar Fourier imaging (SPFI), and then extracted diffusion orientations coinciding with neural fiber tracts. Only under angular constraints, the deterministic path planning algorithm was subsequently used to find all reasonable pathways between pairwise white matter (WM) voxels in different regions of interest (ROIs). Consequently, a train of consecutive WM voxels along each of the identified pathways was determined, and the connection strength of these pathways was computed by integrating their EAP alignment over a solid angle. The connection strength of a pair of WM voxels was assigned as the connection strength with the largest connection possibility. Finally, the connection strength between two ROIs was calculated as the sum of all the connection probabilities of each pair of WM voxels in the ROIs. A comparison against voxel-graph based probabilistic tractography method was performed on Fibercup phantom dataset, and the results demonstrated that the proposed method can produce better structural connection and is more computationally economical. Lastly, three datasets from Human Connectome Project (HCP) S1200 group were tested and their structural connectivity networks were constructed for topological analysis. The results showed great consistency in network metrics with previous WM network studies in healthy adults.

1. Introduction

Due to aging population, aging-related brain pathologies have been on the rise and demand advanced diagnostic technology to improve our understanding of brain functions. As multiple pathologies are associated with impairments in structural connectivity of brain, a detailed structural connectivity map covering entire brain would be of great value for neuroscience [1]. In addition, some brain diseases such as Schizophrenia and Alzheimer's Disease involve aberrant topology of structural connectivity network of the brain [2,3]. Accurate network-based analysis on structural connectivity can also lead to powerful imaging markers for brain diseases. Despite the pitfalls that limits anatomical connection accuracy, tractography based on diffusion weighted imaging (DWI) is still the most promising method for building structural connectivity network at macroscopic level [4].

Global tractography is a mathematical framework, which aims to address the ill-posed nature of the diffusion tractography by modeling it as a global inverse problem. However, those techniques are computationally demanding and have not become widespread yet [5]. Currently, there are two main categories of algorithms to construct structural connectivity network of human brain from DWI data – the deterministic algorithm and the probabilistic algorithm [6,7]. The deterministic algorithm follows the main fiber directions revealed by the diffusion model and generate sequences of points that are considered as fibers. Specifically, streamline-based deterministic algorithms delineate fiber pathways by tracking diffusion directions with a step size [8–10]. However, it is challenging for these algorithms to achieve accurate fiber tracking results in regions where fibers cross or branch. Consequently,

---

[*] Corresponding author. Department of Biomedical Engineering, University of Houston, 4849 Calhoun Rd., Rm 373, Houston, TX, 77004, USA.
E-mail address: yzhang94@uh.edu (Y. Zhang).

https://doi.org/10.1016/j.compbiomed.2019.103384
Received 24 May 2019; Received in revised form 25 July 2019; Accepted 4 August 2019

the brain connectivity strength measured from the number of fibers may not be robust. Moreover, the noise and partial volume effect in DWI would increase the uncertainty of fiber pathways, as they could initiate a meaningless change in pathways. On the contrary, probabilistic algorithms usually repeat many times the deterministic version by randomly perturbing the main fiber directions, and produce maps of connectivity, which indicate the probability that a given voxel is connected to a reference position. Using a probabilistic algorithm, paths along aberrant orientations tend to disperse quickly because voxels along these paths are classified with a low probability. However, although probabilistic tractography algorithms show a good resistance to fiber path uncertainty in constructing brain structural connectivity, spurious WM connections that are not anatomically connected may be induced. Considering these limitations, it is beneficial to strategically utilize the strengths from these two algorithms to further improve the structural connection while still maintaining an economical computational cost.

In this study, a new structural connectivity construction method utilizing the strengths of both deterministic and probabilistic algorithms was developed. First, all reasonable paths connecting seed and target voxels are identified according to the orientations extracted from the Ensemble Average Propagator (EAP), an emerging method to characterize tissue microstructure that, to our best knowledge, has not been thoroughly investigated in the construction of brain structural connectivity network currently [11]. Next, the probabilities of these paths were estimated by integrating EAP alignment along them over a solid angle, and the strongest path was regarded as a real neural fiber connection. The connectivity strength between brain regions was then estimated by summing up the connection possibility of each pair of WM voxels. Thus, a non-directed weighted structural network was established with brain regions as nodes, and connection strengths as arc weights.

2. Methods

2.1. Ensemble average propagator (EAP)

EAP is a full three-dimensional displacement probability function of water molecules in brain tissues, which could faithfully characterize the water diffusion process in brain tissues [12,13]. Compared with two traditional methods, diffusion tensor (DT) [14–22] and orientation distribution function (ODF) [23–26], EAP preserves the radial part of the diffusion signal and therefore has the potential to accurately identify crossing orientations of neural fascicles contained in a WM voxel [11,27,28]. It was reported that EAP profile usually has a superior ability to characterize main diffusion directions than ODF [29,30]. The relationship between diffusion signal attenuation and EAP is given by a Fourier transform (FT) relationship [12].

$$P(\mathbf{R}) = \int_{\boldsymbol{q}\in\mathbb{R}^3} \frac{S(\boldsymbol{q})}{S_0} e^{2\pi i \boldsymbol{q}\cdot\boldsymbol{R}} d\boldsymbol{q} \tag{1}$$

where $S(\mathbf{q})$ is the diffusion signal measured at position $\mathbf{q}$ in q-space, and S_0 is the baseline image acquired without any diffusion sensitization. $\mathbf{R}$ is the diffusion displacement vector.

In this study, spherical polar Fourier imaging (SPFI) was employed to estimate EAP from multi-shell DWI samples [29]. The implementation includes two steps. The first step is to estimate coefficients from attenuated signals and the second step is the linear analytical transform. SPFI uses analytical transforms to avoid numerical Fourier transform and numerical integral in diffusion spectrum imaging in order to achieve high computational efficiency. EAP is calculated along every direction after spherical harmonic (SH) coefficients are acquired. Compared with Q-ball imaging, which works only for single shell data, SPFI works for arbitrarily sampled data. Compared with DSI, SPFI requires a smaller number of samples and lower b values [31,32]. In Refs. [27,28], two EAP-based streamline-like tractography algorithms are proposed, showing the advantage of the EAP-tract method over the ODF-tract method. We consider that structural connectivity construction could benefit from EAP.

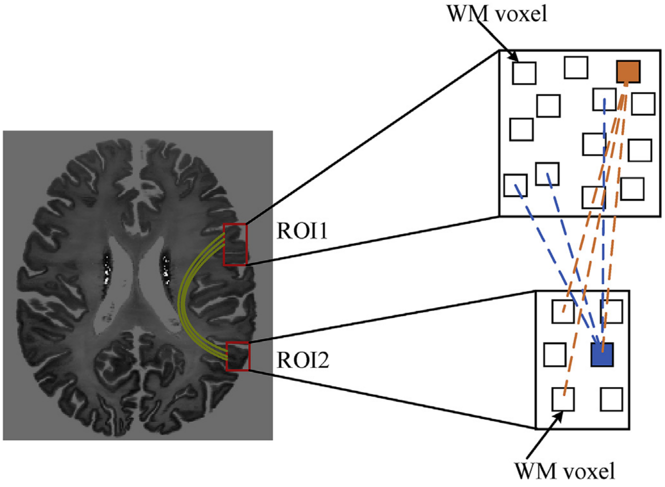

Fig. 1. Diagram of the connection probability computation between two ROIs. The connection strength between two ROIs (marked with red rectangles) were estimated by summing up all the connection possibility of each pair of WM voxels (such as the colored voxels) in the two ROIs. If no link is found between them, their connection strength is assigned to zero. Here, ROIs denote brain functional areas. In this study, the cerebral cortex was actually parcellated into 68 regions.

2.2. Structural connection strength

The direction of maximal diffusion is assumed to coincide with the direction of fiber tracts [33–36]. After deriving EAPs using SPFI, diffusion directions contained in a WM voxel are extracted through detecting local peaks of EAP [37]. These orientations are used to identify reasonable paths between each pair of WM voxels in ROIs. A path is viewed as a serial of consecutive WM voxels, linking a seed voxel to a target one.

The definition of an index of structural connectivity is a topic of great interest in the neuroscience community. Links are defined between spatially adjacent WM voxels. The strength (weight) of a link is chosen so that it could represent the probability that neighboring voxels are really connected by neural fibers. According to Refs. [23,24,38], the weight of a link is estimated as follows.

$$w_{ij} = w_{ji} = P(\boldsymbol{i}, \boldsymbol{r}_{ij}) + P(\boldsymbol{j}, \boldsymbol{r}_{ji}) \tag{2}$$

where $P(\boldsymbol{i}, \boldsymbol{r}_{ij})$ is a pseudo-probability term of diffusing from WM voxel $\boldsymbol{i}$ along the direction $\boldsymbol{r}_{ij}$ that connects the centers of voxel $\boldsymbol{i}$ and $\boldsymbol{j}$. Similarly, it can be given by integrating the EAP over a solid angle ω around the vector $\boldsymbol{r}_{ij}$ as shown in equation (3). The angle ω is determined by the neighborhood system, and the $3 \times 3 \times 3$ neighborhood ($\omega = \frac{4\pi}{26}$) is used in this study.

$$P(\boldsymbol{i}, \boldsymbol{r}_{ij}) = \frac{1}{Z}\int_{\omega} EAP(\boldsymbol{i}, \boldsymbol{r})dS \approx \frac{1}{Z}\sum_{q=1}^{Q} EAP(\boldsymbol{i}, \boldsymbol{r}_q)\cdot\Delta S_q \tag{3}$$

where Z is a normalization constant set to $\frac{Pij_{max}}{2}$, Q is the number of diffusion directions distributing in ω. The strength M of a fiber bundle path $[(\boldsymbol{i}_1, \boldsymbol{i}_2), (\boldsymbol{i}_2, \boldsymbol{i}_3), \cdots, (\boldsymbol{i}_{X-1}, \boldsymbol{i}_X)]$ that comprises of N WM voxels $\boldsymbol{i}_1, \boldsymbol{i}_2, \cdots, \boldsymbol{i}_N$ is given by:

$$M = w_{\boldsymbol{i}_1,\boldsymbol{i}_2}\cdot w_{\boldsymbol{i}_1,\boldsymbol{i}_2}\cdot\ldots\cdot w_{\boldsymbol{i}_{N-1},\boldsymbol{i}_N} \tag{4}$$

When all reasonable paths are identified between seed and target WM voxels using deterministic path planning algorithm, the probability of the strongest path is assigned as the connection strength between

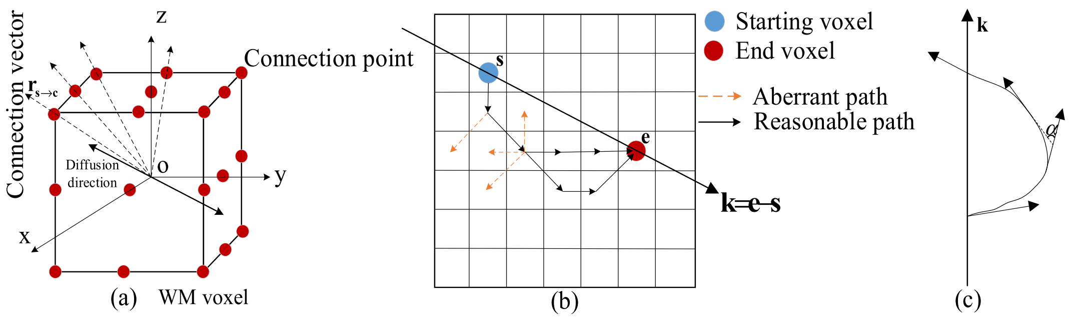

Fig. 2. Diagram of identifying the paths between seed and target WM voxels. (a) Among 26 neighboring WM voxels (red dots indicate the 26-connected voxels), we choose the voxel whose connecting vector (dotted line) is most aligned with the diffusion direction (solid line) as the next consecutive voxel. For the sake of simplicity, only four dotted lines were outlined. (b) Here, for the sake of representability, we considered 2D tracts from *s* to *e*. There are two paths connecting *s* and *e*. (c) The angle between two successive directions cannot be larger than the threshold α_{th}.

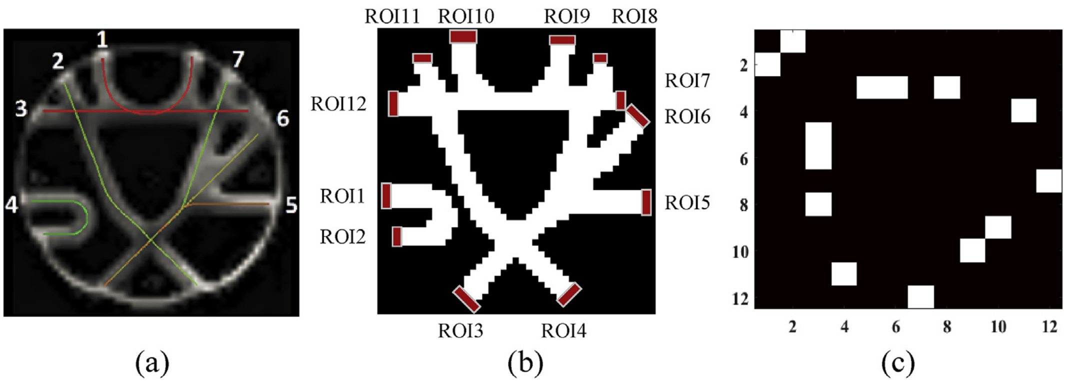

Fig. 3. Ground truth of Fibercup fiber pathways. (a) The phantom consists of 7 fiber bundles, including crossing, branching, and bending bundles. In (b), the dark red regions are ROIs for estimating connection strength, which are drawn manually. The white pixels in the connection map (c) just show that there is fiber connections between two ROIs, and cannot denote connection strength.

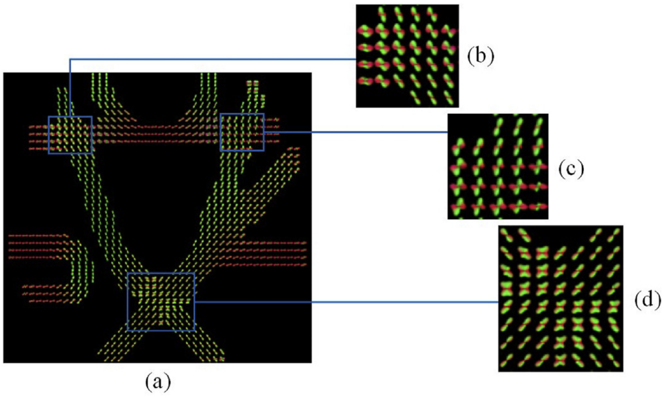

Fig. 4. EAP field constructed using SPFI with the parameters as R = 0.015 mm, SH order = 4, and Rad order = 1 [29]. The crossing regions in (a) were marked out with blue rectangles, and the enlarged views were displayed as (b), (c), and (d), respectively. Compared with ground truth of Fiberup phantom, the local peaks of EAPs coincide with fiber orientations.

them through direct comparisons instead of graph-based searching. The connection strength between two different regions is finally estimated by summing up the probability of each pair of WM voxels (equation (5)). Such a probability-based approach could reduce spurious WM connections that are not anatomically connected. The structural connection strength between any two brain functional regions is defined as:

$$S(ROI_1, ROI_2) = \sum_{\boldsymbol{i}\in ROI_1} w(\boldsymbol{i}, ROI_2) + \sum_{\boldsymbol{i}\in ROI_2} w(\boldsymbol{j}, ROI_1) \tag{5}$$

where the term $w(\boldsymbol{i}, ROI_2)$ denotes the connectivity probability of a WM voxel $\boldsymbol{i} \in ROI_1$ with each WM voxel in ROI_2. Similarly, $w(\boldsymbol{j}, ROI_1)$ denotes the connectivity of WM voxel $\boldsymbol{j} \in ROI_2$ with each WM voxel ROI_1. Note that the right first term in equation (5) quantifies connection strength between ROI_2 with ROI_1, and the right second term quantifies connection strength between ROI_1 with ROI_2 (Fig. 1). The detailed process of estimating the connection strength between seed and target WM voxels is described as follow.

Input: seed voxel $\boldsymbol{s}$ in ROI1, target voxel $\boldsymbol{e}$ in ROI2 (see Fig. 1).

Output: Path connection probability.

(1) Compute EAPs from single- or multi-shell samples in q-space using SPFI [29–31].

(2) Extract diffusion orientations through detecting local peaks of EAPs.

(3) For each diffusion direction $\boldsymbol{v}$ in voxel $\boldsymbol{s}$, identify the next consecutive voxel in its 26 neighbor WM voxels. As shown in Fig. 2(a), the neighbor voxel $\boldsymbol{c}$ is retained as the next consecutive voxel of $\boldsymbol{v}$ if $\boldsymbol{r}_{\boldsymbol{s}\to\boldsymbol{c}}$ (dotted line in Fig. 2(a)) is most aligned with $\boldsymbol{v}$ (solid line in Fig. 2(a)).

$$\boldsymbol{c} = \underset{\boldsymbol{c}}{argmin}\, \boldsymbol{r}_{\boldsymbol{s}\to\boldsymbol{c}}\cdot\boldsymbol{v} \tag{6}$$

where $\boldsymbol{r}_{\boldsymbol{s}\to\boldsymbol{c}}$ is the vector pointing from the center of $\boldsymbol{s}$ to the center of $\boldsymbol{c}$.

(4) Choose the diffusion directions satisfying equation (7) contained in voxel $\boldsymbol{c}$ for the next propagation.

$$\left\{ \boldsymbol{d}_p \middle| \arccos\left(\frac{\boldsymbol{v}\cdot\boldsymbol{d}_p}{|\boldsymbol{v}||\boldsymbol{d}_p|}\right) < \alpha_{th},\ p = 1,2,\cdots,N \right\} \tag{7}$$

where $\boldsymbol{d}_p$ is the diffusion direction in $\boldsymbol{c}$, and N is the number of diffusion directions in $\boldsymbol{c}$. α_{th} is the angle between the successive vectors along the

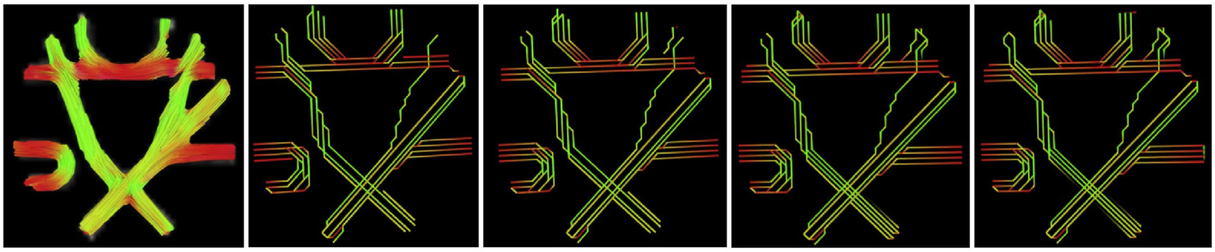

Whole-phantom stream-line tracts

Connection paths between 12 ROIs at angular constraint of 30°

Connection paths between 12 ROIs at angular constraint of 50°

Connection paths between 12 ROIs at angular constraint of 70°

Connection paths between 12 ROIs at angular constraint of 90°

Fig. 5. Whole-phantom streamline tracts and connection paths between 12 ROIs at different angular constraint of 30°, 50°, 70° and 90°. These paths only represent connection relationship between ROIs, instead of realistic tracts. The WM voxels consecutively distributed on the paths would be used to compute the connection weight between ROIs.

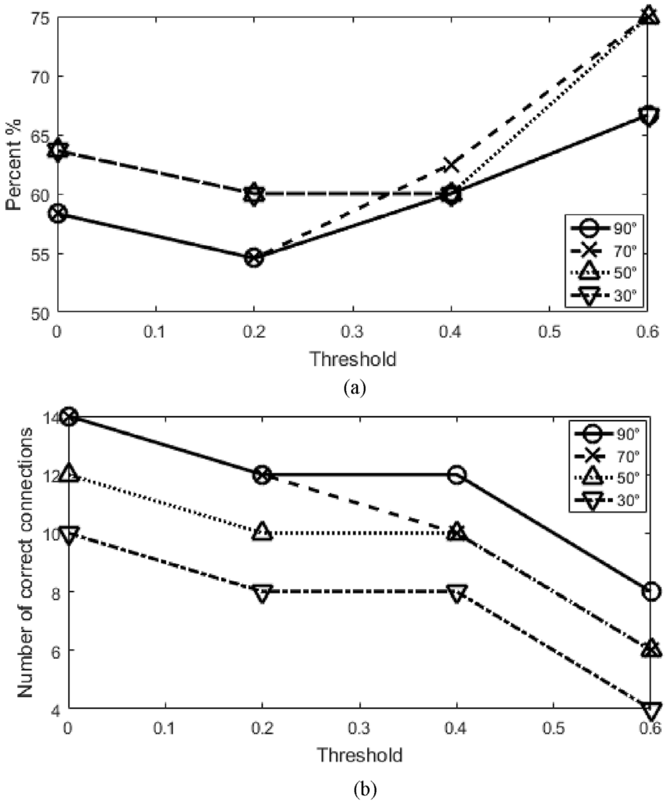

Fig. 6. Comparison across different angular constraints, including $\alpha_{th} = 90°$, $\alpha_{th} = 70°$, $\alpha_{th} = 50°$, and $\alpha_{th} = 30°$. (a) Correct rate in percent at different angular constraints. (b) Number of correct connections at different angular constraints.

same path (Fig. 2(c)).

(5) $s = c$, go to (3). Iterate until non-WM region is met or there are no directions satisfying equation (7). By checking if there were the same indexes of voxels in a path, circle fibers would be removed.

(6) Identify the paths that can reach e, and compute their connection probabilities according to equation (4). Assign the probability of the strongest path as the connectivity strength between **s** and **e**. For example, there are two paths between **s** and **e** in Fig. 2(b), the stronger path would be considered as the connection. If no reasonable paths are found, the connection strength between s and e is set to zero.

At last, structural connection strength between two ROIs is estimated according to equation (5).

The calculated structural connection strengths depend on the alignment of EAP along the path between each pair of WM voxels, with higher strengths indicating better alignments. The connection strength derived from EAPs could be more robust and suitable for structural connectivity network topological analysis. After the connectivity matrix is obtained, human brain can be modeled as a non-directed weighted graph. The topologic characteristics of brain structural connectivity networks can be further investigated with graph theory. In this study, we first test the proposed method on Fibercup dataset, and then applied it to construct human brain structural connectivity network, and investigated the network metrics including network efficiency, small-worldness, hub regions, and backbone links.

3. Results

3.1. Phantom dataset

The proposed method was first evaluated using the Fibercup phantom dataset. The dataset consists of 2 acquisitions, each acquired at 3 different b-values (650 s/mm^2, 1500 s/mm^2, 2000 s/mm^2). Parameters for the 3 mm isotropic acquisition were as follows: field of view FOV = 19.2 cm, matrix 64 × 64, slice thickness TH = 3 mm, read bandwidth RBW = 1775 Hz/pixel, partial Fourier factor = 6/8, parallel reduction factor GRAPPA = 2, repetition time TR = 5s, 2 repetitions. Three diffusion sensitizations at b = 650/1500/2000 s/mm^2 corresponding to the echo times TE = 77/94/102 ms respectively were used. Three slices were acquired. A signal-noise ratio (SNR) of 15.8 was measured for the baseline (b = 0) image. SNR of DWI at b = 650/1500/2000 s/mm^2 were evaluated at 9.1/2.6/1.12, respectively [39–41]. Fig. 3 (a) shows the ground truth of the fiber bundles in this phantom, including crossing, branching, and bending bundles [42]. Fig. 3 (b) shows 12 seed ROIs (dark red rectangles) marked on WM mask. The white pixels in Fig. 3 (c) only indicate connections between any two ROIs, not connection strength.

SPFI was employed to estimate EAP. Fig. 4 illustrates the EAP field of Fibercup phantom. The DWI signals were sampled along 64 diffusion directions uniformly distributed on a spherical shell. Before EAP construction, we denoised this dataset using MRtrix3 [43]. The parameters for EAP construction are set as R = 0.015 mm, SH order = 4, and Rad order = 1 [29]. In Fig. 4(a), the orientations of crossing and branching fibers were identified definitely, and the enlarged views were shown in Fig. 4(b), (c), and (d).

In the proposed method, the structural connectivity construction was influenced by the angular threshold α_{th} between successive directions. To investigate its impact, we applied different angular values for α_{th}, including 90°, 70°, 50°, and 30°. Fig. 5 shows whole-phantom streamline tracts and connection paths between 12 ROIs at different angular constraint of 30°, 50°, 70° and 90°. These paths only represent connection relationship between ROIs, instead of realistic tracts. The

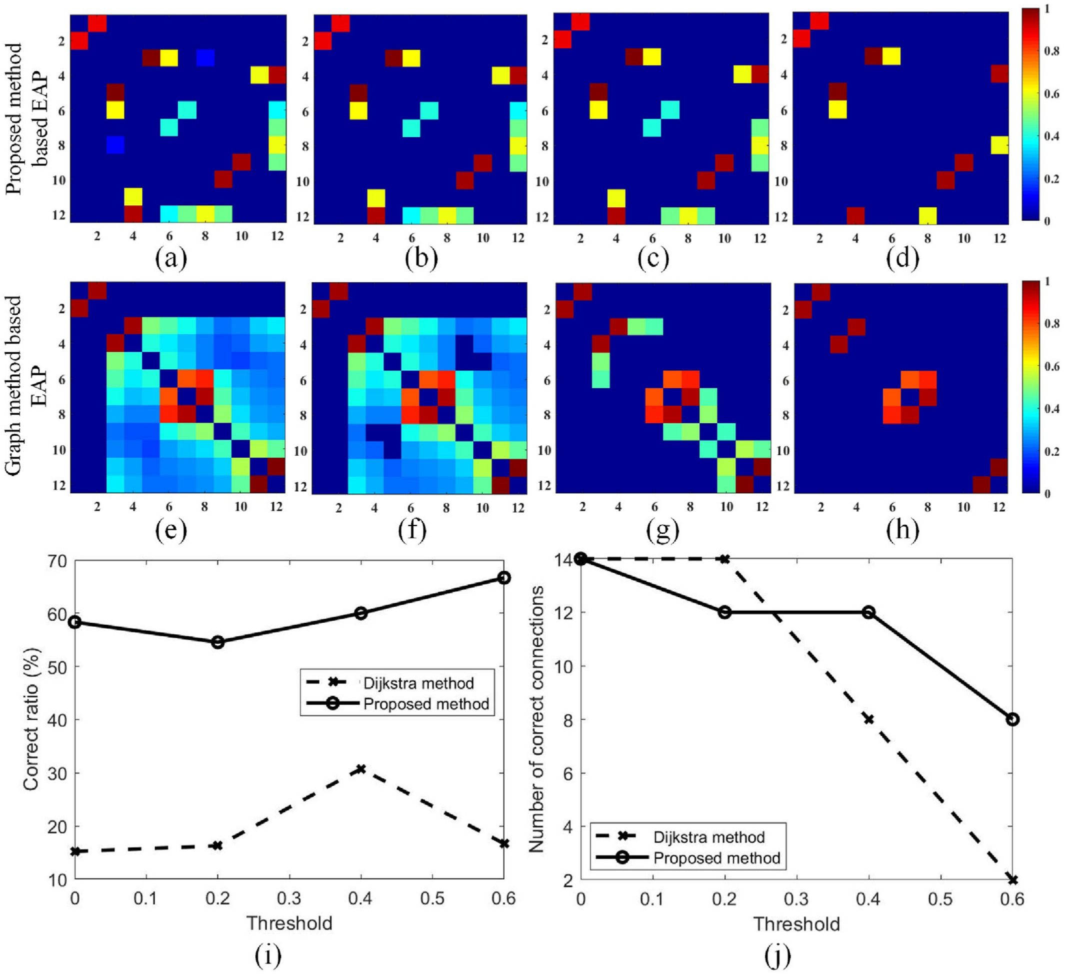

Fig. 7. Structural connectivity of Fibercup phantom dataset. Top row is the connection map constructed with our proposed method, and bottom row is computed using graph-based method present in Refs. [7,23]. (a) and (e) are the original connection maps. (b) and (f) are the maps filtered at the threshold of 0.2. (c) and (g) are the maps filtered at the threshold of 0.4. (d)) and (h) are the maps filtered at the threshold of 0.6. (i) shows the ratio of correct connections, and (j) illustrates the number of correct connections.

Table 1
Cerebral cortex parcellation including 68 regions, 34 per hemisphere.

Left hemisphere		Right hemisphere	
1. Bankssts	18. Para hippocampal	35. Bankssts	52. Para hippocampal
2. Caudal anterior cingulate	19. Parsopercularis	36. Caudal anterior cingulate	53. Parsopercularis
3. Caudal middle frontal	20. Parsorbitalis	37. Caudal middle frontal	54. Parsorbitalis
4. Cuneus	21. Pars triangularis	38. Cuneus	55. Pars triangularis
5. Entorhinal	22. Pericalcarine	39. Entorhinal	56. Pericalcarine
6. Frontal pole	23. Post central	40. Frontal pole	57. Post central
7. Fusiform	24. Posterior cingulate	41. Fusiform	58. Posterior cingulate
8. Inferior parietal	25. Precentral	42. Inferior parietal	59. Precentral
9. Inferior temporal	26. Precuneus	43. Inferior temporal	60. Precuneus
10. Insula	27. Rostral anterior cingulate	44. Insula	61. Rostral anterior cingulate
11. Isthmus cingulate	28. Rostral middle frontal	45. Isthmus cingulate	62. Rostral middle frontal
12. Lateral occipital	29. Superior frontal	46. Lateral occipital	63. Superior frontal
13. Lateral orbitofrontal	30. Superior parietal	47. Lateral orbitofrontal	64. Superior parietal
14. Lingual	31. Superior temporal	48. Lingual	65. Superior temporal
15. Medial orbitofrontal	32. Supra marginal	49. Medial orbitofrontal	66. Supra marginal
16. Middle temporal	33. Temporal pole	50. Middle temporal	67. Temporal pole
17. Paracentral	34. Transverse temporal	51. Paracentral	68. Transverse temporal

The indexes for pacellated regions are coded from 1 for bankssts of left hemisphere to 68 for transverse temporal of right hemisphere in turn [46]. The indexes from 35 to 68 are assigned to the parcellated regions of right hemisphere in the same order.

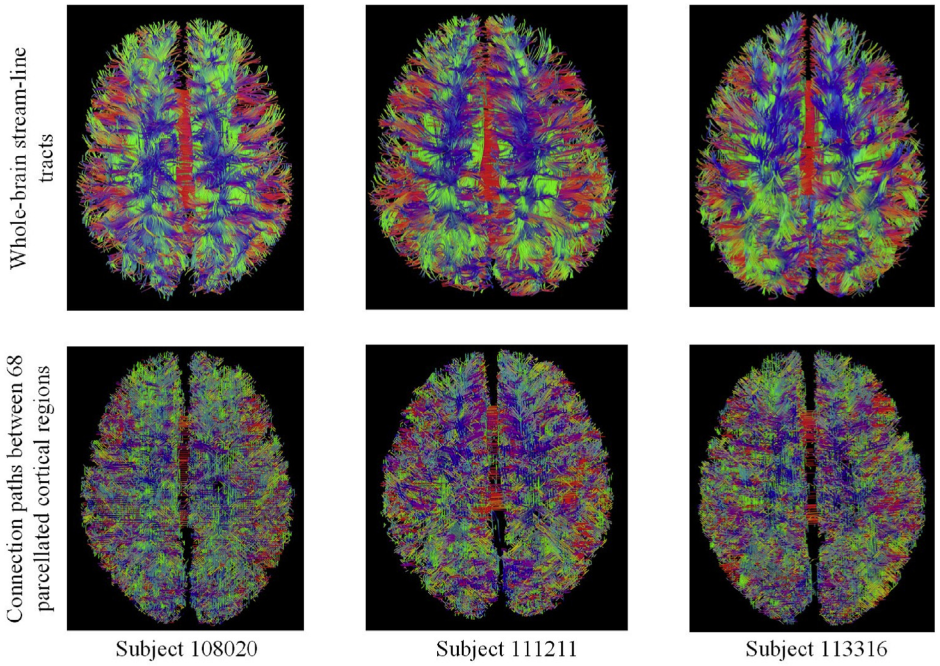

Fig. 8. Whole-brain streamline tracts and connection paths between 68 parcellated cortical regions. These paths just denote connection relationship between ROIs, instead of realistic WM tracts. The WM voxels consecutively distributed on the paths would be used to compute the connection weight between ROIs.

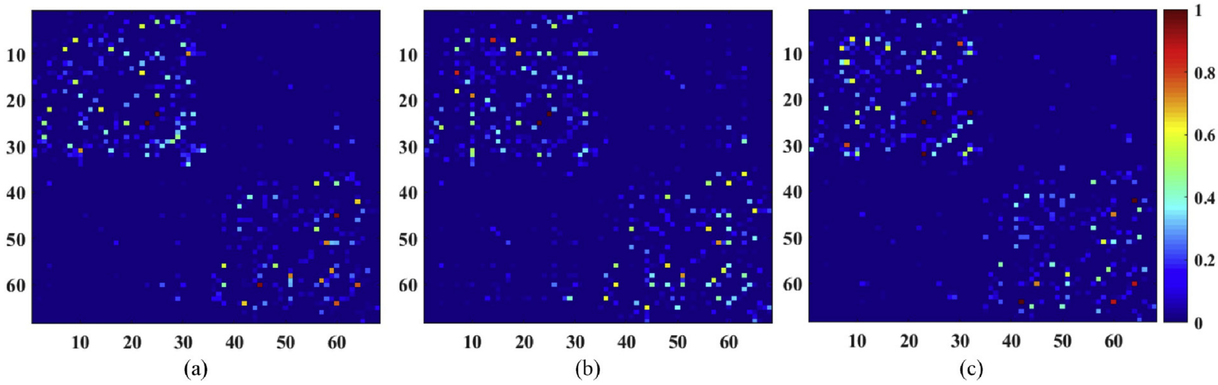

(a) (b) (c)

Fig. 9. Structural connectivity maps of three HCP S1200 subjects constructed with the proposed method. (a) Subject of 108020. (b) Subject of 111211. (c) Subject of 113316.

Table 2
Structural network metrics were analyzed, including $\boldsymbol{E_g}$, $\boldsymbol{E_{loc}}$, $\boldsymbol{C_p}$, $\boldsymbol{L_p}$, $\boldsymbol{\gamma}$, $\boldsymbol{\lambda}$, and $\boldsymbol{\sigma}$.

Subject ID	E_g	E_{loc}	C_p	L_p	γ	λ	σ
108020	0.0618	0.1151	0.0742	16.1584	5.1510	1.2227	4.2127
111211	0.0668	0.1612	0.0913	14.9642	4.9926	1.1941	4.1810
113316	0.0620	0.1191	0.0754	16.1214	5.4422	1.2832	4.2409
Mean	0.0635	0.1318	0.0803	15.7480	5.1952	1.2333	4.2115

WM voxels consecutively distributed on the paths would be used to compute the connection weight between ROIs. The comparison across different angular constraints was shown in Fig. 6. As for $\alpha_{th} = 70°$ and $\alpha_{th} = 50°$, the correct rate was up to 75% at strength threshold of 0.6. For $\alpha_{th} = 30°$, the correct rate showed minimal changes at different thresholds. At $\alpha_{th} = 90°$, the correct rate remained the same as $\alpha_{th} = 70°$ at the thresholds of 0 and 0.2, and the same as $\alpha_{th} = 30°$ at the thresholds of 0.4 and 0.6. The number of correct connections was largest at $\alpha_{th} = 90°$.

In order to confirm the advantage of the proposed method over Dijkstra searching, under the condition of $\alpha_{th} = 90°$, our method was used to construct the connection map of Fibercup phantom based on EAP. The distance_weifunction proposed in brain connectivity toolbox (BCT) [44] was used to compute the connection weight between any two ROIs for the method in Ref. [23]. Fig. 7 (a)~(h) illustrates the connections estimated based on EAP at the connection thresholds of 0, 0.2, 0.4, and 0.6. Fig. 7 (i) and (j) indicated that the connections established with our method match the ground truth better (54.55%–66.67% vs 15.22%–30.77%). At the thresholds of 0.4 and 0.6, the number of correct connections derived from proposed method were greater than Dijkstra method (12 vs 8 and 8 vs 2, respectively).

3.2. *In-vivo datasets*

The human brain datasets from the Washington University-University of Minnesota consortium of the Human Connectome Project (HCP; http://www.humanconnectome.org) were used in this study to further characterize the performance of the proposed method. DWI images were acquired with 288 gradient directions distributed on three shells (b value = 1000 s/mm^2, 2000 s/mm^2, 3000 s/mm^2), with the following scanning parameters: TR = 5520 ms, TE = 89.5 ms, flip

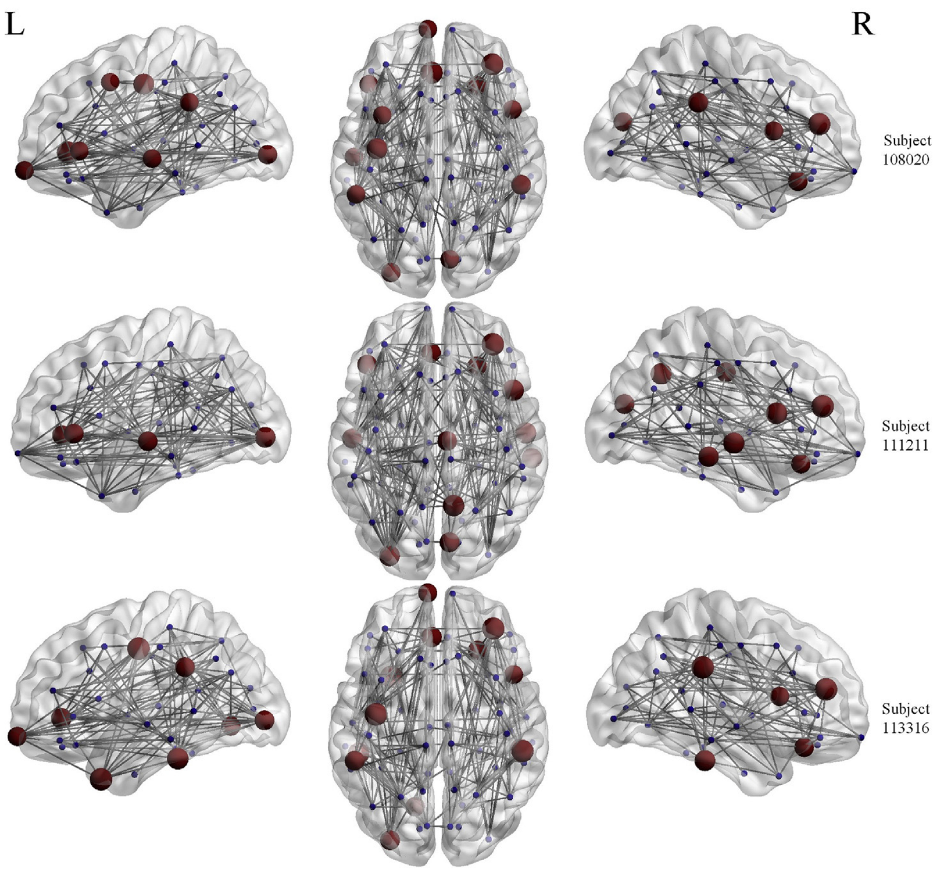

Fig. 10. Hub regions of HCP subjects. The hub nodes were obtained according to nodal efficiency values. The nodes were considered brain hubs if their nodal efficiencies were at least 1 SD greater than the average nodal efficiency of the network. The brain graphs were visualized using BrainNet Viewer software [52]. The dark red nodes indicate hub regions.

Table 3
Hub regions of structural networks. The hub region name refers to Table 1.

Subject ID	Hub regions (ROI index)
108020	3/10/20/23/25/29/30/31/38/45/51/60/64
111211	10/19/25/29/38/45/48/51/56/58/60/63
113316	8/10/13/23/25/30/31/32/42/45/51/60/64

angle = 78, FOV = 1584 × 1848mm^2, and voxel size = 1.25 mm isotropic. T1-weighted structural image was acquired with the following parameters: TR = 2400 ms, TE = 2.14 ms, flip angle = 8, FOV = 320 × 320mm2, 256slices, and voxel size = 0.7 mm isotropic [45]. The datasets of three healthy adults from HCP S1200 group were used to verify the proposed method, including two males (22–25 y) and one female (26–30 y).

High-resolution (259 × 259 × 310) T1-weighted MRI images were used to extract the brain, and different brain tissues such as gray matter, white matter, cerebrospinal fluid (CSF) were further segmented out. Cerebral cortex was parcellated into 68 functional areas, 34 cortical regions per hemisphere (Table 1) [46]. At last, corresponding atlas were affine registered to DWI native space (144 × 144 × 173). All operations were accomplished in Freesurfer 6.0.0. In this experiment, to force anatomically realistic path propagation, a 90° maximum curvature threshold ($\alpha_{th} = 90°$) was imposed between two successive path steps [23]. Fig. 8 shows whole-brain streamline tracts and connection paths between 68 parcellated cortical regions. These paths just denote connection relationship between different cortical regions, instead of realistic WM tracts. The WM voxels consecutively distributed on the paths would be used to compute the connection weight between ROIs. Fig. 9 shows the structural connectivity maps of the HCP S1200 subjects. The connection weights were normalized to [0, 1].

After the connectivity networks were retrieved, their network topological properties were investigated with the tool of GRETNA [47] and BCT [44]. The calculated network metrics were summarized in Table 2, including the metrics of E_g, E_{loc}, C_p, L_p, γ, λ, and σ (see Refs. [48–51] for detailed definitions). Briefly, the global efficiency E_g measures the global efficiency of the parallel information transfer in brain network. The local efficiency E_{loc} reveals how efficient the communication is among the neighbors of a node when it is removed. The clustering coefficient C_p indicates the extent of local interconnectivity or cliquishness in brain network. L_p is the shortest path length of a network. γ, λ, and σ are small-world parameters. The results confirm the small-world attributes of human brain structural network, satisfying the small-world conditions of λ~1, $\gamma \gg 1$, and $\sigma > 1$.

The hub nodes of these three networks were illustrated in Fig. 10, and the hub node indexes were listed in Table 3. The nodes were considered brain hubs if their nodal efficiencies were at least 1 standard deviation greater than the average nodal efficiency of the network. Nodal efficiency measures the average shortest path length between a given node and all of the other nodes in brain network. These brain graphs were visualized using BrainNet Viewer software [52].

According to Fig. 7 (i) and (j), the proposed method showed a better performance than traditional method with a connection threshold set at 0.4. Here, we further extracted the backbone connections from the constructed networks at the threshold of 0.4. Fig. 11 shows the backbone connections. These brain graphs were visualized using BrainNet Viewer software [52]. The red links denote backbone connections, and the radius represents connection strength. The common backbone connections of the subjects are list in Table 4.

4. Discussion

This study presented an EAP-based method extended from Refs. [7,23] to directly build human brain structural connectivity networks, combining deterministic path planning and probabilistic connection

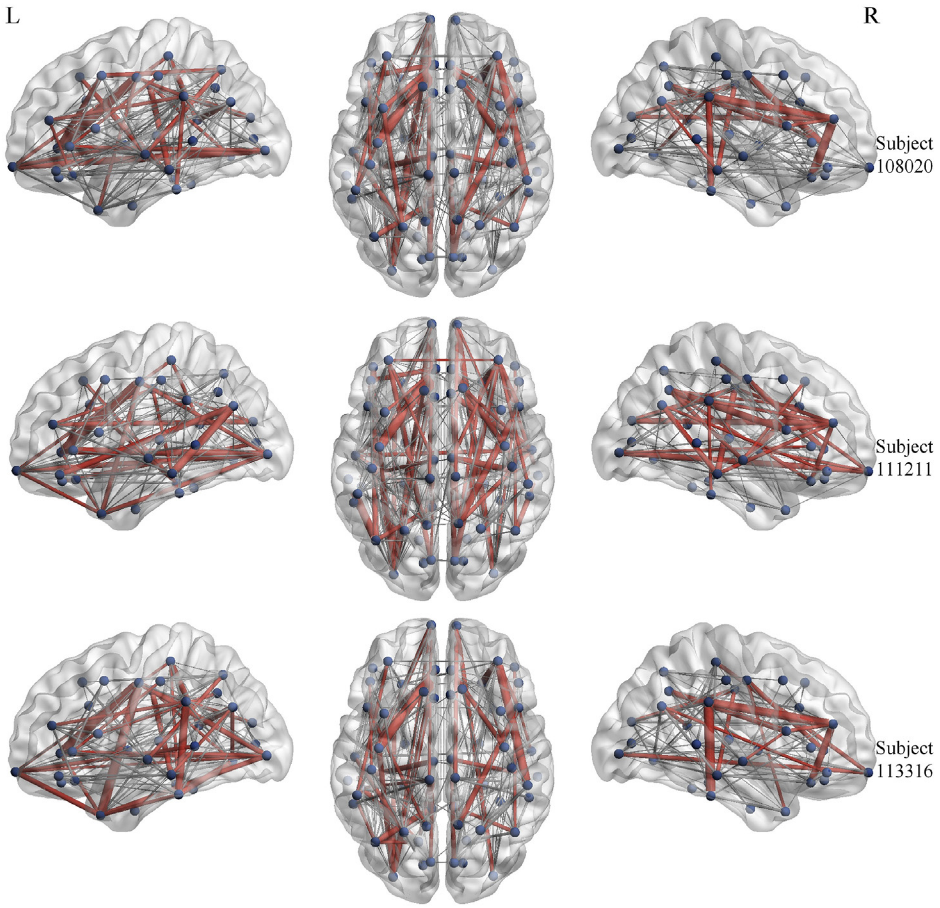

Fig. 11. The backbone connections of the three subjects. The connection strength threshold is 0.4. The brain graphs were visualized using BrainNet Viewer software [52]. The red links denote backbone connections, and the radius represents connection strength.

Table 4
Common backbone connections at the threshold of 0.4 across the three subjects.

Connections/(region index, region index)
(4, 22), (7, 9), (9, 16), (10, 19), (10, 25), (10, 31), (14, 22), (16, 31), (23, 25), (23, 32), (38, 56), (42, 64), (44, 65), (45, 60), (48, 56), (51, 58), (51, 60), (57, 59), (60, 64)

strength estimation. Compared to Refs. [7,23], the tracking algorithm in this study utilized determined path planning to obtain reasonable structural connections for connection strength estimation. The results showed a markedly improved accuracy, with reduced computational cost compared to Dijkstra method.

One main contribution of this study was that it strategically combined the advantages of deterministic and probabilistic algorithms. As the two main categories of the connectivity strength method, deterministic and probabilistic algorithms have been previously reported in the literature [6]. However, these two algorithms come with inherent limitations. For example, regarding deterministic algorithms, the construction of human brain connectivity network is directly dependent on the results of deterministic tracking, and the accuracy suffers from fiber path uncertainty induced by noise and partial volume effect. To address this issue, some geometrical methods have been proposed to calculate connectivity strength between different brain regions based on diffusion tensor and ODF fields [14–16]. Regarding the probabilistic algorithms, in Refs. [7,23], a framework based on ODF and voxel-graph theory was proposed to construct structural brain connectivity network. The defined brain graph was searched exhaustively to identify the strongest paths among nodes. In Ref. [24], ODFs were decomposed into components representative of single-fiber populations and a multigraph was created for retrieving the strongest paths and assigning connectivity strengths between each particular seed and all the other voxels. However, because of the huge number of white matter (WM) voxels in human brain DWI datasets, the computation of the connecting matrix may be very time- and memory-consuming.

Another contribution of our study was that we employed EAP to extract fiber orientations and to compute path strength, which can more faithfully reflect diffusion profile. Both DT and ODF have been used to estimate the connection strength between different brain areas [14–22]. The DT assumes a displacement probability characterized by Gaussian distribution function, and it has limited capacity to resolve multiple crossings inside a voxel [53,54]. The ODF is well known to represent the angular structure of the diffusion. However, it also has some limitations. First, the radial integration over a solid angle is done all over EAP, and thus is likely to catch unwanted artifact that leads to false orientation detection [27–29]. Second, fiber bundles with large differences in anisotropy are difficult to be identified when the partial volume effect in DWI is high [55]. As such, there still remain open questions concerning the accurate estimation of connectivity strength from DWI data. In future, it is necessary to comprehensively assess different effects of EAP and ODF on brain structural connectivity network. To date, several methods have been reported to recover EAP profile, including harmonic oscillator with exponential penalty [27], Laplace equation [12], Hermite Polynomials [13], and spherical polar Fourier imaging (SPFI) [29]. Specifically, SPFI provides a model-free analytical EAP reconstruction, with better robustness and greater efficiency, and it was employed to retrieve EAP from multiple-shell DWI samples.

The validation performed on Fibercup phantom dataset shows that the proposed method achieves better structural connections (see Fig. 7). In Refs. [7,23,24], a Dijkstra searching algorithm was used to acquire the strongest path linking two WM voxels. However, there are two shortcomings in this approach: first, it is liable to induce false structural connections; second, the exhaustive search becomes more time-consuming and memory-consuming with the growth of the number of WM voxels in DWI data. The advantage of the proposed method is in reducing strengths of less anatomically plausible connections through the deterministic path planning. It is also relatively fast and avoids a full searching in a non-directed voxel-wise graph, a problem of [7,23,24].

To verify the applicability of the proposed method in in-vivo clinical utility, three in-vivo datasets of healthy adults from HCP S1200 group were used to construct brain structural networks. We used Desikan-Killiany atlas as a reference map for brain parcellation, and totally 68 brain regions (34 regions for each hemisphere) were regarded as the nodes of the connectivity network [46]. The connectivity adjacent matrices are shown in Fig. 9. And the topological properties were also investigated, including efficiency (E_g and E_{loc}), small-world attributes (γ $\lambda\sigma$), clustering coefficient (C_p), shortest path length (L_p), hub regions, and backbone connections. The results (Table 2) confirm the small-world attributes of human brain structural network. The parameters of interest are $\lambda_{mean} = 1.2333$, $\gamma_{mean} = 5.1952$ and $\sigma_{mean} = 4.2115$, satisfying the small-world conditions of $\lambda\sim1$, $\gamma \gg 1$, and $\sigma > 1$ [56,57]. According to Ref. [33], brain structural networks present bigger local efficiency and smaller global efficiency, and our results ($E_g^{mean} = 0.0635$ and $E_{loc}^{mean} = 0.1318$) agree with this statement. However, it is worth to note that the values of these topological parameters would be different when cortex parcellation scheme changes.

The hub regions distributed in the SC networks are identified for each subject (Fig. 10). The nodes were considered brain hubs if their nodal efficiencies were at least 1 standard deviation greater than the average nodal efficiency of the network. We found that the subjects showed similar hub distributions, including the common hub regions of lateral occipital (left hemisphere), rostral anterior cingulate (left hemisphere), lateral orbitofrontal (right hemisphere), pars opercularis (right hemisphere), and rostral middle frontal (right hemisphere). This finding is largely consistent with previous structural network studies in healthy adults [58–61].

Lastly, the backbone connections of structural connectivity networks were extracted from the networks constructed based on EAP (Figs. 11), and 19 common backbone connections were identified across them (Table 4). There are three backbone connections passing through the function regions of lateral occipital (left hemisphere) and rostral middle frontal (right hemisphere). There are two backbone connections passing through the regions of isthmus cingulate (left hemisphere), paracentral (left hemisphere), posterior cingulate (left hemisphere), rostral anterior cingulate (left hemisphere), precentral (left hemisphere), frontal pole (left hemisphere), posterior cingulate (right hemisphere), and supra marginal (right hemisphere). These backbone connections mainly account for whole brain communication.

5. Conclusion

A new method for structural connectivity network construction was developed in this study that integrated the probabilistic and deterministic algorithms based on EAP. Compared to the traditional algorithm, the proposed algorithm showed greatly improved accuracy in structural connections and high computational efficiency. Future work would aim to improve the quality and robustness of structural connectivity networks, such as enhancing the precision of connectivity strength estimation.

Conflicts of interest

None Declared.

Acknowledgement

The research is supported by Natural Science Foundation of Zhejiang Province (LY17E070007), China, and National Natural Science Foundation of China (51207038), and the University of Houston. Human brain datasets were provided by the Human Connectome Project, WU-Minn Consortium (Principal Investigators: David Van Essen and Kamil Ugurbil; 1U54MH091657) funded by the 16 NIH Institutes and Centers that support the NIH Blueprint for Neuroscience Research; and by the McDonnell Center for Systems Neuroscience at Washington University.

References

[1] P. Hagmann, M. Kurant, X. Gigandet, P. Thiran, V.J. Wedeen, R. Meuli, J. Thiran, Mapping human whole-brain structural networks with diffusion MRI, PLoS One 2 (2007) e597 https://doi.org/10.1371/journal.pone.0000597.

[2] M.P. van den Heuvel, R.C.W. Mandl, C.J. Stam, R.S. Kahn, H.E.H. Pol, Aberrant frontal and temporal complex network structure in Schizophrenia: a graph theoretical analysis, J. Neurosci. 30 (2010) 15915–15926 https://doi.org/10.1523/jneurosci.2874-10.2010.

[3] Z. Dai, C. Yan, K. Li, Z. Wang, J. Wang, M. Cao, Q. Lin, N. Shu, M. Xia, Y. Bi, Y. He, Identifying and mapping connectivity patterns of brain network hubs in Alzheimer's disease, Cerebr. Cortex 25 (2014) 3723–3742 https://doi.org/10.1093/cercor/bhu246.

[4] K.G. Schilling, V. Nath, C.B. Hansen, P. Parvathaneni, J.A. Blaber, Y. Gao, P.F. Neher, D.B. Aydogan, Y. Shi, M. Ocampopineda, S. Schiavi, A. Daducci, G. Girard, M. Barakovic, J. Rafaelpatino, D. Romascano, G. Rensonnet, M. Pizzolato, A. Bates, E. Fischi, J. Thiran, E.J. Canalesrodriguez, C. Huang, H. Zhu, L. Zhong, R.P. Cabeen, A.W. Toga, F. Rheault, G. Theaud, J.C. Houde, J. Sidhu, M. Chamberland, C. Westin, T.B. Dyrby, R. Verma, Y. Rathi, M.O. Irfanoglu, C. Thomas, C. Pierpaoli, M. Descoteaux, A.W. Anderson, B.A. Landman, Limits to anatomical accuracy of diffusion tractography using modern approaches, Neuroimage 185 (2018) 1–11 https://doi.org/10.1016/j.neuroimage.2018.10.029.

[5] A. Hamamci, Cellular Automata Tractography Fast Geodesic Diffusion MR Tractography and Connectivity Based Segmentation on the GPU, Neuroinformatics (2019) 1–17 https://doi.org/10.1007/s12021-019-09425-y.

[6] M. Descoteaux, R. Deriche, T.R. Knosche, A. Anwander, Deterministic and probabilistic tractography based on complex fibre orientation distributions, IEEE Trans. Med. Imaging 28 (2009) 269–286 https://doi.org/10.1109/TMI.2008.2004424.

[7] M. Cieslak, T. Brennan, W. Meiring, L.J. Volz, C. Greene, A. Asturias, S. Suri, S.T. Grafton, Analytic tractography: a closed-form solution for estimating local white matter connectivity with diffusion MRI, Neuroimage 169 (2018) 473–484 https://doi.org/10.1016/j.neuroimage.2017.12.039.

[8] S. Mori, B.J. Crain, V.P. Chacko, P.C.M. Van Zijl, Three-dimensional tracking of axonal projections in the brain by magnetic resonance imaging, Ann. Neurol. 45 (1999) 265–269 https://doi.org/10.1002/1531-8249(199902)45:2 < 265::AID-ANA21 > 3.0.CO;2-3.

[9] Y. Chao, J. Chen, K. Cho, C. Yeh, K. Chou, C. Lin, A multiple streamline approach to high angular resolution diffusion tractography, Med. Eng. Phys. 30 (2008) 989–996 https://doi.org/10.1016/j.medengphy.2008.01.010.

[10] P. Fillard, M. Descoteaux, A. Goh, S. Gouttard, B. Jeurissen, J.G. Malcolm, A. Ramirezmanzanares, M. Reisert, K.E. Sakaie, F. Tensaouti, T. Yo, J. Mangin, C. Poupon, Quantitative evaluation of 10 tractography algorithms on a realistic diffusion MR phantom, Neuroimage 56 (2011) 220–234 https://doi.org/10.1016/j.neuroimage.2011.01.032.

[11] D. Varadarajan, J.P. Haldar, A theoretical signal processing framework for linear diffusion MRI: implications for parameter estimation and experiment design, Neuroimage 161 (2017) 206–218 https://doi.org/10.1016/j.neuroimage.2017.08.048.

[12] M. Descoteaux, R. Deriche, D. Le Bihan, J. Mangin, C. Poupon, Multiple q-shell diffusion propagator imaging, Med. Image Anal. 15 (2011) 603–621 https://doi.org/10.1016/j.media.2010.07.001.

[13] A. Ghosh, R. Deriche, Fast and closed-form ensemble-average-propagator approximation from the 4th-order diffusion tensor, IEEE International Symposium on Biomedical Imaging. 2010, 2010, pp. 1105–1108 https://doi.org/10.1109/ISBI.2010.5490186.

[14] H. Li, Z. X, K. Cui, S.T.C. Wong, Diffusion tensor-based fast marching for modeling human brain connectivity network, Comput. Med. Imag. Graph. 35 (2011) 167–178 https://doi.org/10.1016/j.compmedimag.2010.07.008.

[15] G.J.M. Parker, C.A.M. Wheeler-Kingshott, G.J. Barker, Estimating distributed anatomical connectivity using fast marching methods and diffusion tensor imaging, IEEE Trans. Med. Imaging 21 (2002) 505–512 https://doi.org/10.1109/TMI.2002.1009386.

[16] J.S.W. Campbell, K. Siddiqi, V.V. Rymar, A.F. Sadikot, G.B. Pike, Flow-based fiber tracking with diffusion tensor and q-ball data: validation and comparison to principal diffusion direction techniques, Neuroimage 27 (2005) 725–736 https://doi.org/10.1016/j.neuroimage.2005.05.014.

[17] O. Friman, G. Farnebäck, C.F. Westin, A Bayesian approach for stochastic white matter tractography, IEEE Trans. Med. Imaging 25 (2006) 965–978 https://doi.org/10.1109/TMI.2006.877093.

[18] R.S. Vorburger, C. Reischauer, P. Boesiger, BootGraph: probabilistic fiber tractography using bootstrap algorithms and graph theory, Neuroimage 66 (2013) 426–435 https://doi.org/10.1016/j.neuroimage.2012.10.058.

[19] T.E.J. Behrens, H. Johansenberg, M.W. Woolrich, S.M. Smith, C.A.M. Wheelerkingshott, P.A. Boulby, G.J. Barker, E.L. Sillery, K. Sheehan, O. Ciccarelli, A.J. Thompson, J.M. Brady, P.M. Matthews, Non-invasive mapping of connections between human thalamus and cortex using diffusion imaging, Nat. Neurosci. 6 (2003) 750–757 https://doi.org/10.1038/nn1075.

[20] Q. Cao, N. Shu, L. An, P. Wang, L. Sun, M. Xia, J. Wang, G. Gong, Y. Zang, Y. Wang, Y. He, Probabilistic diffusion tractography and graph theory analysis reveal abnormal white matter structural connectivity networks in drug-naive boys with attention deficit/hyperactivity disorder, J. Neurosci. 33 (2013) 10676–10687 https://doi.org/10.1523/JNEUROSCI.4793-12.2013.

[21] V.L. Galinsky, L.R. Frank, Simultaneous multi-scale diffusion estimation and tractography guided by entropy spectrum pathways, IEEE Trans. Med. Imaging 34 (2015) 1177–1193 https://doi.org/10.1109/TMI.2014.2380812.

[22] G. Gong, Y. He, L. Concha, C. Lebel, D.W. Gross, A.C. Evans, C. Beaulieu, Mapping anatomical connectivity patterns of human cerebral cortex using in vivo diffusion tensor imaging tractography, Cerebr. Cortex 19 (2009) 524–536 https://doi.org/10.1093/cercor/bhn102.

[23] Y. Iturria-Medina, E.J. Canalesrodríguez, L. Meliegarcía, P.A. Valdeshernandez, E. Martinezmontes, Y. Alemangomez, J.M. Sanchezbornot, Characterizing brain anatomical connections using diffusion weighted MRI and graph theory, Neuroimage 36 (2007) 645–660 https://doi.org/10.1016/j.neuroimage.2007.02.012.

[24] S.N. Sotiropoulos, L. Bai, P.S. Morgan, C.S. Constantinescu, C.R. Tench, Brain tractography using Q-ball imaging and graph theory: improved connectivities through fibre crossings via a model-based approach, Neuroimage 49 (2010) 2444–2456 https://doi.org/10.1016/j.neuroimage.2009.10.001.

[25] J.I. Berman, S. Chung, P. Mukherjee, C.P. Hess, E.T. Han, R.G. Henry, Probabilistic streamline q-ball tractography using the residual bootstrap, Neuroimage 39 (2008) 215–222 https://doi.org/10.1016/j.neuroimage.2007.08.021.

[26] S.N. Sotiropoulos, L. Bai, P.S. Morgan, C.S. Constantinescu, C.R. Tench, Brain tractography using Q-ball imaging and graph theory: improved connectivities through fibre crossings via a model-based approach, Neuroimage 49 (2010) 2444–2456 https://doi.org/10.1016/j.neuroimage.2009.10.001.

[27] S. Merlet, A. Philippe, R. Deriche, M. Descoteaux, Tractography via the ensemble average propagator in diffusion MRI, International Conference on Medical Image Computing and Computer-Assisted Intervention, 2012, pp. 339–346 https://doi.org/10.1007/978-3-642-33418-4_42.

[28] G. Girard, R. Fick, M. Descoteaux, R. Deriche, D. Wassermann, AxTract: microstructure-driven tractography based on the ensemble average propagator, International Conference on Information Processing in Medical Imaging, 2015, pp. 675–686 https://doi.org/10.1007/978-3-319-19992-4_53.

[29] J. Cheng, A. Ghosh, T. Jiang, R. Deriche, Model-free and analytical EAP reconstruction via spherical polar Fourier diffusion MRI, International Conference on Medical Image Computing and Computer-Assisted Intervention, 2010, pp. 590–597 https://doi.org/10.1007/978-3-642-15705-9_72.

[30] J. Cheng, R. Deriche, T. Jiang, D. Shen, P.T. Yap, Non-negative spherical deconvolution (NNSD) for estimation of fiber orientation distribution function in single/multi-shell diffusion MRI, Neuroimage 101 (2014) 750–764 https://doi.org/10.1016/j.neuroimage.2014.07.062.

[31] S. Xie, L. Chen, N. Zuo, T. Jiang, DiffusionKit: a light one-stop solution for diffusion MRI data analysis, J. Neurosci. Methods 273 (2016) 107–119 https://doi.org/10.1016/j.jneumeth.2016.08.011.

[32] J. Cheng, A. Ghosh, R. Deriche, T. Jiang, Model-free, regularized, fast, and robust analytical orientation distribution function estimation, medical image computing computer assisted intervention, (2010), pp. 648–656 https://doi.org/10.1007/978-3-642-15705-9_79.

[33] D.B. Le, R. Turner, P. Douek, Is water diffusion restricted in human brain white matter? An echo-planar NMR imaging study, Neuroreport 4 (1993) 887–890 https://doi.org/10.1097/00001756-199307000-00012.

[34] J.D. Tournier, F. Calamante, D.G. Gadian, A. Connelly, Direct estimation of the fiber orientation density function from diffusion-weighted MRI data using spherical deconvolution, Neuroimage 23 (2004) 1176–1185 https://doi.org/10.1016/j.neuroimage.2004.07.037.

[35] K.E. Sakaie, M.J. Lowe, An objective method for regularization of fiber orientation distributions derived from diffusion-weighted MRI, Neuroimage 34 (2007) 169–176 https://doi.org/10.1016/j.neuroimage.2006.08.034.

[36] K.M. Otto, H.H. Ehricke, V. Kumar, U. Klose, Angular smoothing and radial regularization of ODF fields: application on deterministic crossing fiber tractography, Eur. J. Med. Plants 29 (2013) 17–32 https://doi.org/10.1016/j.ejmp.2011.10.002.

[37] Z. Wu, X. Yu, Y. Liu, M. Hong, A PSO-Powell hybrid method to extract fiber orientations from ODF, Comput. Math. Methods Med. (2018) 1–12 https://doi.org/10.1155/2018/7680164.

[38] Y. Iturria-Mmedina, R.C. Sotero, E.J. Canalesrodríguez, Y. Alemangomez, L. Meliegarcia, Studying the human brain anatomical network via diffusion-weighted MRI and graph theory, Neuroimage 40 (2008) 1064–1076 https://doi.org/10.1016/j.neuroimage.2007.10.060.

[39] M. Cote, A. Bore, G. Girard, J. Houde, M. Descoteaux, Tractometer: Online Evaluation System for Tractography, Medical Image Computing and Computer Assisted Intervention, (2012), pp. 699–706 https://doi.org/10.1007/978-3-642-33415-3_86.

[40] P. Fillard, M. Descoteaux, A. Goh, S. Gouttard, B. Jeurissen, J.G. Malcolm, A. Ramirezmanzanares, M. Reisert, K.E. Sakaie, F. Tensaouti, T. Yo, J. Mangin, C. Poupon, Quantitative evaluation of 10 tractography algorithms on a realistic diffusion MR phantom, Neuroimage 56 (2011) 234-220 https://doi.org/10.1016/j.neuroimage.2011.01.032.

[41] C. Poupon, B. Rieul, I. Kezele, M. Perrin, F. Poupon, J.F. Mangin, New diffusion phantoms dedicated to the study and validation of HARDI models, Magn. Reson. Med. 60 (2008) 1276–1283 https://doi.org/10.1002/mrm.21789.

[42] M.A. Côté, G. Girard, A. Boré, E. Garyfallidis, J. Houde, M. Descoteaux, Tractometer: towards validation of tractography pipelines, Med. Image Anal. 17 (2013) 844–857 https://doi.org/10.1016/j.media.2013.03.009.

[43] J. Veraart, E. Fieremans, D.S. Novikov, Diffusion MRI noise mapping using random matrix theory, Magn. Reson. Med. 76 (2015) 1582–1593 https://doi.org/10.1002/mrm.26059.

[44] M. Rubinov, O. Sporns, Complex network measures of brain connectivity: uses and interpretations, Neuroimage 52 (2010) 1059–1069 https://doi.org/10.1016/j.neuroimage.2009.10.003.

[45] D.C. Van Essen, S.M. Smith, D.M. Barch, T.E.J. Behrens, E. Yacoub, K. Ugurbil, The Wu-Minn human connectome project: an overview, Neuroimage 80 (2013) 62–79 https://doi.org/10.1016/j.neuroimage.2013.05.041.

[46] R.S. Desikan, F. Ségonne, B. Fischl, B.T. Quinn, B.C. Dickerson, D. Blacker, R.L. Buchner, A.M. Dale, R.P. Maguire, B.T. Hyman, M.S. Albert, R.J. Killiany, An automated labeling system for subdividing the human cerebral cortex on MRI scans into gyral based regions of interest, Neuroimage 31 (2006) 968–980 https://doi.org/10.1016/j.neuroimage.2006.01.021.

[47] J. Wang, X. Wang, M. Xia, X. Liao, A. Evans, Y. He, GRETNA: a graph theoretical network analysis toolbox for imaging connectomics, Front. Hum. Neurosci. 9 (2015) 386 https://doi.org/10.3389/fnhum.2015.00386.

[48] Q. Cao, N. Shu, L. An, P. Wang, L. Sun, M. Xia, J. Wang, G. Gong, Y. Zang, Y. Wang, Y. He, Probabilistic diffusion tractography and graph theory analysis reveal abnormal white matter structural connectivity networks in drug-naive boys with attention deficit/hyperactivity disorder, J. Neurosci. 33 (2013) 10676–10687 https://doi.org/10.1523/JNEUROSCI.4793-12.2013.

[49] Y. He, A. Evans, Graph theoretical modeling of brain connectivity, Curr. Opin. Neurol. 23 (2010) 341–350 https://doi.org/10.1097/WCO.0b013e32833aa567.

[50] G. Gong, Y. He, L. Concha, C. Lebel, D.W. Gross, A.C. Evans, C. Beaulieu, Mapping anatomical connectivity patterns of human cerebral cortex using in vivo diffusion tensor imaging tractography, Cerebr. Cortex 19 (2008) 524–536 https://doi.org/10.1093/cercor/bhn102.

[51] Y. Li, Y. Liu, J. Li, W. Qin, K. Li, C. Yu, T. Jiang, Brain anatomical network and intelligence, PLoS Comput. Biol. 5 (2009) e1000395https://doi.org/10.1371/journal.pcbi.1000395.

[52] M. Xia, J. Wang, Y. He, BrainNet viewer: a network visualization tool for human brain connectomics, PLoS One 8 (2013) e68910https://doi.org/10.1371/journal.pone.0068910.

[53] P. Mukherjee, J.I. Berman, S.W. Chung, C.P. Hess, R.G. Henry, Diffusion tensor MR imaging and fiber tractography: theoretic underpinnings, Am. J. Neuroradiol. 29 (2008) 632–641 https://doi.org/10.3174/ajnr.A1051.

[54] E. Özarslan, T.M. Shepherd, B.C. Vemuri, S.J. Blackband, T.H. Mareci, Resolution of complex tissue microarchitecture using the diffusion orientation transform (DOT), Neuroimage 31 (2006) 1086–1103 https://doi.org/10.1016/j.neuroimage.2006.01.024.

[55] D. Acqua, F. Scifo, P. Rizzo, G. Catani, M. Simmons, A. Scotti, G. Fazio, A modified damped Richardson–Lucy algorithm to reduce isotropic background effects in spherical deconvolution, Neuroimage 49 (2010) 1446–1458 https://doi.org/10.1016/j.neuroimage.2009.09.033.

[56] D.J. Watts, S.H. Strogatz, Collective dynamics of small-world networks, Nature 393 (1998) 440–442 https://doi.org/10.1038/30918.

[57] M.D. Humphries, K. Gurney, T.J. Prescott, The brain stem reticular formation is a small-world, not scale-free, network, Proc. Biol. Sci. 273 (2006) 503–511 https://doi.org/10.1098/rspb.2005.3354.

[58] P. Hagmann, L. Cammoun, X. Gigandet, R. Meuli, C.J. Honey, V.J. Wedeen, O. Sporns, Mapping the structural core of human cerebral cortex, PLoS Biol. 6 (2008) e159 https://doi.org/10.1371/journal.pbio.0060159.

[59] M.P. van den Heuvel, O. Sporns, Rich-club organization of the human connectome, J. Neurosci. 31 (2011) 15775–15786 https://doi.org/10.1523/JNEUROSCI.3539-11.2011.

[60] G. Gong, P. Rosa-Neto, F. Carbonell, Z.J. Chen, Y. He, A.C. Evans, Age and gender-related differences in the cortical anatomical network, J. Neurosci. 29 (2009) 15684–15693 https://doi.org/10.1523/JNEUROSCI.2308-09.2009.

[61] M.P. van den Heuvel, R.S. Kahn, J. Goñi, O. Sporns, High-cost, high-capacity backbone for global brain communication, Proc. Natl. Acad. Sci. 109 (2012) 11372–11377 https://doi.org/10.1073/pnas.1203593109.